

# Analyzing the Effects of Key Design Factors of a Negative-Differential-Resistance (NDR) Microfluidic Oscillator—an Equivalent-Circuit-Model Approach

J. W. Wu<sup>1</sup>, H. M. Xia<sup>1,\*</sup>, Z. P. Wang<sup>2</sup>, W. Wang<sup>2</sup> and H. J. Du<sup>3</sup>

<sup>1</sup> School of Mechanical Engineering, Nanjing University of Science and Technology, Nanjing, Jiangsu 210094, China

<sup>2</sup> Singapore Institute of Manufacturing Technology, 73 Nanyang Drive, Singapore 637662, Singapore

<sup>3</sup> School of Mechanical and Aerospace Engineering, Nanyang Technological University, 50 Nanyang Avenue, Singapore 639798, Singapore

Received 18 August 2021; Accepted (in revised version) 13 October 2021

---

**Abstract.** Numerical study on dynamic hydroelastic problems is usually rather complex due to the coupling of fluid and solid mechanics. Here, we demonstrate that the performance of a hydroelastic microfluidic oscillator can be analyzed using a simple equivalent circuit model. Previous studies reveal that its transition from the steady state to the oscillation state follows the negative-differential-resistance (NDR) mechanism. The performance is mainly determined by a bias fluidic resistor, and a pressure-variant resistor which further relates to the bending stiffness of the elastic diaphragm and the depth of the oscillation chamber. In this work, a numerical study is conducted to examine the effects of key design factors on the device robustness, the applicable fluid viscosity, the flow rate, and the transition pressure. The underlying physics is interpreted, providing a new perspective on hydroelastic oscillation problems. Relevant findings also provide design guidelines of the NDR fluidic oscillator.

**AMS subject classifications:** 76-10

**Key words:** Microfluidic oscillator, hydroelastics, equivalent circuit model, negative differential resistance.

---

## 1 Introduction

Microfluidic manipulation is an important topic in the studies of the fast developing micro total analysis system ( $\mu$ -TAS) and microreactor technologies [1, 2]. Due to the inherent low-Reynolds number ( $Re$ ) flow characteristics at micro-scales, special techniques

---

\*Corresponding author.  
Email: hmxia@njjust.edu.cn (H. Xia)

are required in the design of microfluidic functional components such as micropump, micromixer, microvalve, etc. [3]. These design methods are commonly categorized into active ones which use external actuators (e.g., using pneumatic, electric, magnetic, acoustic, optical, centrifugal forces) [4–6], and passive ones by dint of specially designed channels [7–9]. Actuators provide better control flexibility, but external electric devices inevitably increase the system complexity. In comparison, passive methods are more reliable but usually require complex channel structures. Therefore, both have their advantages and limits.

Some atypical microfluidic designs incorporate deformable elastic materials. These devices operate in the passive way, i.e., at constant inlet conditions, they can provide sophisticated flow controls [10–13]. Without resorting to external resources, their operation attributes to the dynamic response of the elastic structures or fluid-structure interaction (FSI) effects. In our previous studies, we reported a hydroelastic microfluidic oscillator which, at a constant driving pressure, produces self-excited oscillation converting a steady laminar flow to oscillatory flow [14, 15]. This device has exhibited great potential in applications such as droplets active control [16], microfiltration enhancement [17], fluid mixing and chemical process intensification [18–21].

The microfluidic oscillator functions through FSI-induced oscillations of an elastic diaphragm, and it is essentially a dynamic hydroelastic problem. Such FSI phenomena are usually rather complex. In traditional studies on macroscopic fluid systems, relevant numerical analysis requires the coupling of CFD (computational fluid dynamic) and mechanical models, and it remains a challenging task today [22–24]. In comparison, for microfluidic devices, their analogy to electric circuits can be utilized to facilitate the design and performance analysis. For above-mentioned hydroelastic microfluidic oscillator, an equivalent circuit model was established, which reveals that it works the way as an electric negative-differential-resistance (NDR) oscillator [25]. A variety of the oscillation behaviors can be interpreted accordingly. The equivalent circuit model of the NDR oscillator provides a facile and alternative method to analyze its characteristics. Especially, it allows direct examination on the effects of the design parameters, and hence greatly reducing the enormous computational resource normally required using CFD methods. This is of significance for device optimization.

In this study, the design space of the NDR microfluidic oscillator is explored numerically using the equivalent circuit model. Relevant analysis and findings provide a new perspective to understand the hydroelastic oscillations in microfluidic systems. It also presents useful design guidelines about how to control its working characteristics to meet specific application requirements, e.g., to process highly viscous fluids, to increase the throughput, etc.

## 2 Key design factors and main characteristics of the NDR oscillator

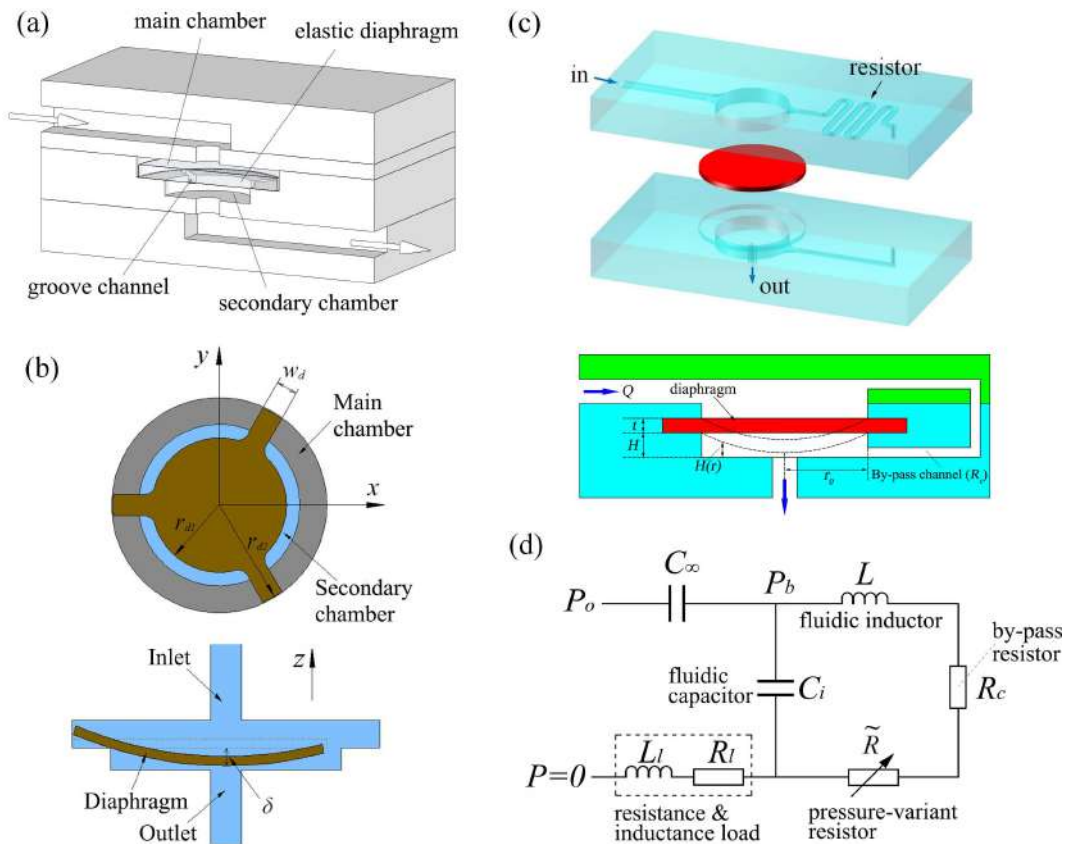


Figure 1: (a)-(c) Different designs of the NDR microfluidic oscillator. In (a), the design utilizes silicone rubber for the oscillating diaphragm which is freely-supported at its edge (Reprinted with permission from reference [14]. Copyright 2012 RSC Publishing). In (b), the diaphragm is made of elastic metal film (Adapted from reference [15]. Copyright 2014 AIP Publishing). The design in (c) also uses silicone rubber, but its edge is fixed and sealed. The fluid flows through a by-pass channel to the downstream (Reprinted with permission from reference [25]. Copyright 2017, IOP Publishing). The sub-figure below is a sectional view of the design. (d) Schematic of an equivalent circuit model of the NDR oscillator.

Figs. 1(a)-(c) present several previously reported NDR microfluidic oscillators that differ in geometrical formats. All the designs include one inlet, one outlet, an oscillation chamber that houses an elastic diaphragm, and a microchannel that crosses over the diaphragm. Essentially, they have the same working mechanism. A sectional view of the third design and its equivalent circuit model are as shown in Figs. 1(c) and (d). Firstly, the microchannel plays the role of a by-pass resistor ( $R_c$ ). With a fluid flow, it will produce an initial bias pressure  $P_b$  that deflects the diaphragm. The chamber and the diaphragm act as a fluidic capacitor  $C_i$ . As the diaphragm oscillates up and down, the fluid will flow in and out, just like the electrical charge and discharge process. When the diaphragm deflects under the bias pressure, it will change the flow resistance. So it also plays the role

of a pressure-variant resistor ( $\tilde{R}$ ). To operate the oscillator, a pressure tank with liquid is applied. By using an auto-regulator, a constant pressure ( $P_o$ ) is applied to drive the liquid out the tank and through the oscillator. Thus, the pressure tank works as a capacitor of infinity ( $C_\infty$ ). Besides, fluidic inductors are used to describe the fluid inertia effects.

At low operating pressure ( $P_o$ ), the diaphragm deflection  $w$  and  $\tilde{R}$  is small, so the flow rate  $Q$  and the bias pressure  $P_b$  are mainly determined by  $R_c$ . According to Darcy-Weisbach equation [26],

$$R_c = \frac{32\rho vl}{AD^2}, \quad (2.1)$$

where  $\rho$  is the fluid density;  $v$  is the fluid kinematic viscosity;  $l$ ,  $A$  and  $D$  are the length, cross-sectional area and hydraulic diameter of the by-pass microchannel respectively. So in the design,  $R_c$  is tunable through changing the length ( $l$ ) and hydraulic diameter ( $D$ ) of the channel.

At large deflections, the elastic diaphragm approaches the bottom of the chamber,  $\tilde{R}$  increases rapidly, which is determined by both the diaphragm deflection  $w$  and the depth of the chamber ( $H$ ) underneath it. The fluid will be accelerated while it flows through the narrow gap between the diaphragm and the chamber bottom (indicated as  $H(r)$  in Fig. 1(c)). The Bernoulli effect becomes significant, producing a load ( $F$ ) to pull the diaphragm further downstream. In addition, how easily the diaphragm deflects under a pressure load relates to its bending stiffness, which is mainly decided by diaphragm Young's modulus  $E$  and thickness  $t$ . Thus, coupling  $E$  or  $t$  with  $H$ ,  $\tilde{R}$  can be tailored for specific design.

The flow rate  $Q = \frac{P_b}{R_b}$ , where the bias resistance  $R_b = R_c + \tilde{R}$ . The differential flow resistance,  $R_{dif} = \frac{dP_b}{dQ}$ . Suppose the load resistance of the oscillator is  $R_l$ , the operating pressure can be calculated as:

$$P_o = Q(R_b + R_l) + \frac{\rho U_o^2}{2}, \quad (2.2)$$

where  $U_o$  is the liquid velocity at the outlet. Above a critical pressure, when  $P_b$  is further increased, the diaphragm deflects so much that it will cause a rapid increase in the flow resistance  $\tilde{R}$ . As a result, the flow rate  $Q$  will decrease.  $R_{dif}$  becomes negative, triggering the oscillation of the elastic diaphragm.

Fig. 2 gives a schematic showing how the flow rate  $Q$ , bias pressure  $P_b$  and differential resistance  $R_{dif}$  change with the diaphragm deflection  $w$ . In our previous numerical study [25], two types of instability are identified, and relevant phenomena are consistent with experimental observations [14, 15]. They are mainly determined by the design parameters and viscosity of the applied fluid.

For both the cases, the flow rate initially increases with  $w$ . After reaching a maximum  $Q_{max}$ , it gradually decreases to 0 at the point  $w_m$  where the diaphragm reaches the bottom of the oscillation chamber and closes the outlet. For  $P_b$ , it exhibits different changing

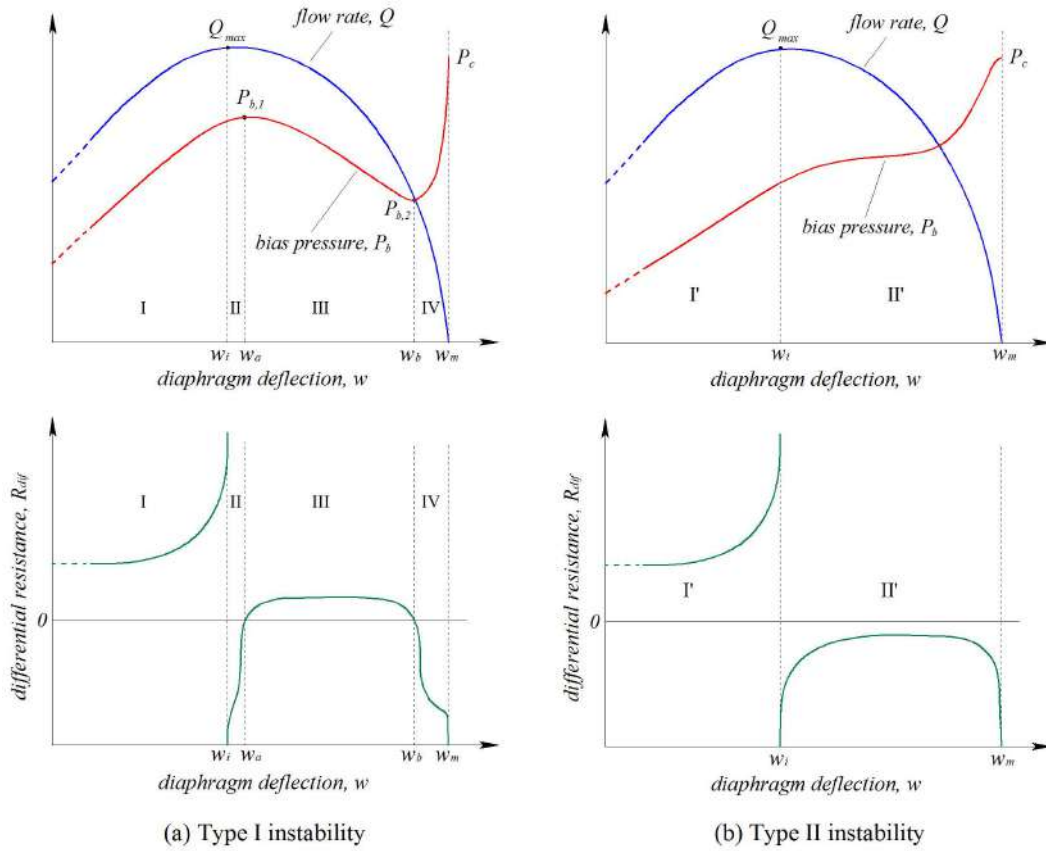


Figure 2: Schematic showing the typical changes of the flow rate  $Q$ , bias pressure  $P_b$  and differential resistance  $R_{dif}$  as a function of the diaphragm deflection  $w$  in a NDR fluidic oscillator. Two different types of instability as shown in (a) and (b) are identified.

trends with  $w$  corresponding to two instability types. For Type I instability, the  $P_b$ - $w$  curve exhibits an N-shaped pattern. Accordingly, based on whether  $R_{dif}$  is positive or negative, the whole deflection range can be divided into four regions. In Regions I ( $w < w_i$ ) and Region III ( $w_a < w < w_b$ ),  $R_{dif} > 0$ . In Regions II ( $w_i < w < w_a$ ) and Region IV ( $w_b < w < w_m$ ),  $R_{dif} < 0$ . Deflection  $w_i$  is the transition point where  $R_{dif}$  turns from positive to negative and the flow system becomes unstable. For type II instability,  $P_b$  increases consistently with  $w$ . As a result, it leads to two different regions over the span of  $w$ —a stable region I' and an unstable region II'. For this case, if the operating pressure  $P_o$  in region II' is less than the pressure required deflecting the diaphragm to close the channel ( $P_c$ ), it may also trigger oscillations. Otherwise, the diaphragm will tend to move to the chamber bottom and stop there, acting as a flow-limiting valve.

According to experimental [14, 15] the oscillator will become less robust when softer materials are used for the diaphragm, or higher-viscosity fluids are applied. Under such

conditions, the applicable fluid viscosity range becomes narrower and the transition pressure is higher. From the simulation results, along with the reduction in the device robustness, the span of region III ( $\Delta w = w_b - w_a$ ) will gradually narrow down and finally disappear, transiting Type I instability to Type II instability. So, an empirical index  $\chi$  is defined here to evaluate the robustness of the device,  $\chi = \Delta w / (w_m - w_i)$ . A large  $\chi$  means a wide workable range of the operating pressure, and high applicable fluid viscosities. On the contrary, small  $\chi$  means the oscillator only works in a narrow pressure range and cannot be applied for high-viscosity fluids. Oscillations can hardly occur at  $\chi = 0$ .

### 3 Methodology

A quasi-static analysis is conducted, which neglects the capacitance and inductance effects. Suppose the diaphragm can reach an equilibrium state at any deflection  $w$ , the corresponding  $P_o$ ,  $P_b$ ,  $Q$ , and  $R_{dif}$  can be calculated. Detailed information about the numerical method was introduced in [25]. It is briefed here to facilitate understanding of the present work.

Firstly, at a given diaphragm deflection  $w$ , the corresponding bias pressure, flow rate, differential flow resistance, etc. can be calculated. It starts from  $w = 0$  with an increment of  $\Delta w = 0.005 \mu m$ . At a deflection  $w$ , the pressure-variant resistance  $\tilde{R}$  can be calculated through integration of the flow resistance over the diaphragm radius

$$\tilde{R} = \int_0^{r_0} \frac{32\rho v}{2\pi r H(r) \cdot D_h(r)^2} dr. \quad (3.1)$$

Here,  $\rho$  is the fluid density,  $v$  is the fluid viscosity,  $r_0$  is the diaphragm radius.  $H(r)$  is the gap between the diaphragm and chamber bottom,  $H(r) = H - w[1 - (\frac{r}{r_0})^2]$ , where  $H$  is the depth of the oscillation chamber.  $D_h(r)$  is the hydraulic diameter at  $r$ ,  $D_h(r) \sim 2H(r)$ .

Then, assume a bias pressure  $P_b$ . Using the thin-plate theory, the corresponding deflection of the diaphragm  $w_1$  can be obtained,

$$\frac{P_b r_0^4}{Et^4} = \frac{5.333}{1-\sigma^2} \frac{w_1}{t} + 1.0815 \left(\frac{w_1}{t}\right)^3, \quad (3.2)$$

where  $E$ ,  $\rho$  and  $t$  are the Young's modulus, Poisson's ratio, and thickness of the diaphragm. With  $\tilde{R}$ ,  $P_b$  and the by-pass resistance  $R_c$ , the flow rate  $Q$  can be calculated as,

$$Q = \frac{P_b}{R_c + \tilde{R}}. \quad (3.3)$$

Next, the central load  $F$  due to Bernoulli effect is calculated as,

$$F = \int_0^{r_0} \frac{\rho}{2} \left(\frac{Q}{2\pi r H(r)}\right)^2 2\pi r \cdot dr. \quad (3.4)$$

The diaphragm deflection caused by  $F(w_2)$  can be obtained through Eq. (3.5)

$$\frac{Fr_0^2}{\pi Et^4} = \frac{1.333}{1-\sigma^2} \frac{w_2}{t} + 0.2948 \left( \frac{w_2}{t} \right)^3. \quad (3.5)$$

The total deflection is approximated as  $w^* = w_1 + w_2$ .

Then based on the difference between  $w^*$  and  $w$ ,  $P_b$  is tuned using the interpolation method. The above procedures are iterated until self-consistent solutions at  $w$  are obtained. The convergence criteria is set as  $|\frac{w^*-w}{w}| < 10^{-12}$ . Then, move on to  $w + \Delta w$  ( $\Delta w = 0.005 \mu m$ ). The differential resistance  $R_{dif}$  is calculated as

$$R_{dif} = \Delta P_b / \Delta Q. \quad (3.6)$$

The evolution of  $R_{dif}$  with  $w$  helps analyze the flow state in the oscillator. The transition point from the steady to oscillatory flow, the required operating pressure, the flow rate range, the applicable viscosity, and reliability of the device can be obtained.

## 4 Results

### 4.1 Influence of the by-pass resistor ( $R_c$ )

The influences of the by-pass resistance are shown in Fig. 3. In this simulation, the other parameters are kept constant. The Young's modulus  $E$  of the diaphragm is 1.52MPa, Poisson's ratio  $\sigma = 0.47$ . The diaphragm thickness  $t = 250 \mu m$  and radius  $r_0 = 0.9 mm$ . The oscillation chamber depth  $H = 300 \mu m$ , and the outlet radius  $r_{out} = 250 \mu m$ . The fluid viscosity is 1cP. For all the cases with different  $R_c$ , the flow rate initially increases and then drops with the deflection of the diaphragm. It also shows that the maximum flow rate  $Q_{max}$  decreases, while the corresponding transition deflection  $w_i$  increases with  $R_c$ . When  $R_c$  increases from  $1.6 \times 10^5 Pa / (ml \cdot s^{-1})$  to  $8.0 \times 10^5 Pa / (ml \cdot s^{-1})$ ,  $Q_{max}$  decreases from 0.44ml/s to 0.12ml/s. Refer to Fig. 3(b), for the design of  $R_c = 1.6 \times 10^5 Pa / (ml \cdot s^{-1})$ ,  $w_i = 265.9 \mu m$ . When  $R_c$  increases to  $8.0 \times 10^5 Pa / (ml \cdot s^{-1})$ ,  $w_i$  increases to 299.1  $\mu m$ . As  $w_i$  shifts to the right, the stable flow Region I expands and the span of Regions II~IV narrows down.

When the diaphragm deflects to the same location that  $w_i = 265.9 \mu m$ , which is the transition point of  $R_c = 1.6 \times 10^5 Pa / (ml \cdot s^{-1})$ , the results of the flow rate  $Q$  and the operating pressure  $P_o$  are shown in Fig. 4(a). When  $R_c$  increases to  $8.0 \times 10^5 Pa / (ml \cdot s^{-1})$ ,  $Q$  decreases from 0.44ml/s to 0.10ml/s. Accordingly, the load  $F$  caused by Bernoulli effect decreases while  $P_o$  increases. This is because that the Bernoulli effect plays an important role to form the  $N$ -shaped  $P_o$ - $w$  curve. With increase of  $R_c$ , the Bernoulli effect become weak and the diaphragm must defect more to trigger the oscillation, i.e., the transition deflection  $w_i$  is increased. Consequently, a higher operating pressure is required. Fig. 4(b) presents the results of transition pressure  $P_i$ , close pressure  $P_c$  and robustness index  $\chi$  with different by-pass resistance  $R_c$ .  $P_c$  is determined by the maximum deflection  $w_m$ , for current case,  $P_c = 111.2 kPa$ . The transition pressure  $P_i$  increases from 80.0kPa to

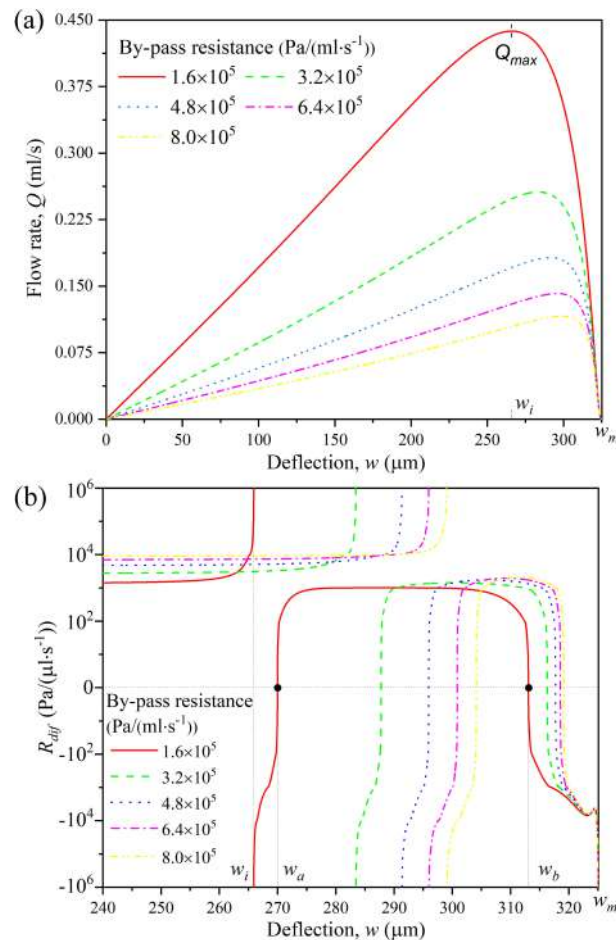


Figure 3: Influence of the by-pass resistance ( $R_c$ ) on the flow rate ( $Q$ ) and the differential flow resistance ( $R_{dif}$ ). (a) Flow rate  $Q$  versus diaphragm deflection  $w$  at different  $R_c$ . (b) The differential flow resistance  $R_{dif}$  versus deflection  $w$  at different  $R_c$ .

96.8kPa over the tested  $R_c$  range. Obviously, the corresponding operating pressure range ( $\Delta P = P_c - P_i$ ) narrows down. In the meanwhile, the robustness index  $\chi$  drops from 0.73 to 0.58.

As the oscillator design with large  $R_c$  becomes less robust, the maximum applicable fluid viscosity  $\mu_{max}$  is accordingly reduced. Relevant results are displayed in Fig. 5. Over the analyzed range of the by-pass channel length ( $l$ ) from 8mm to 40mm,  $\mu_{max}$  drops from 3.6cP to 2.2cP, while the corresponding transition pressure  $P_i$  increases from about 98.8kPa to 101.7kPa. This can be explained as follows. For a large  $R_c$ , a small flow rate  $Q$  can produce a high bias pressure  $P_b$ . While the diaphragm deflects downstream under  $P_b$ , the flow rate  $Q$  may not be high enough to cause significant Bernoulli effects which are

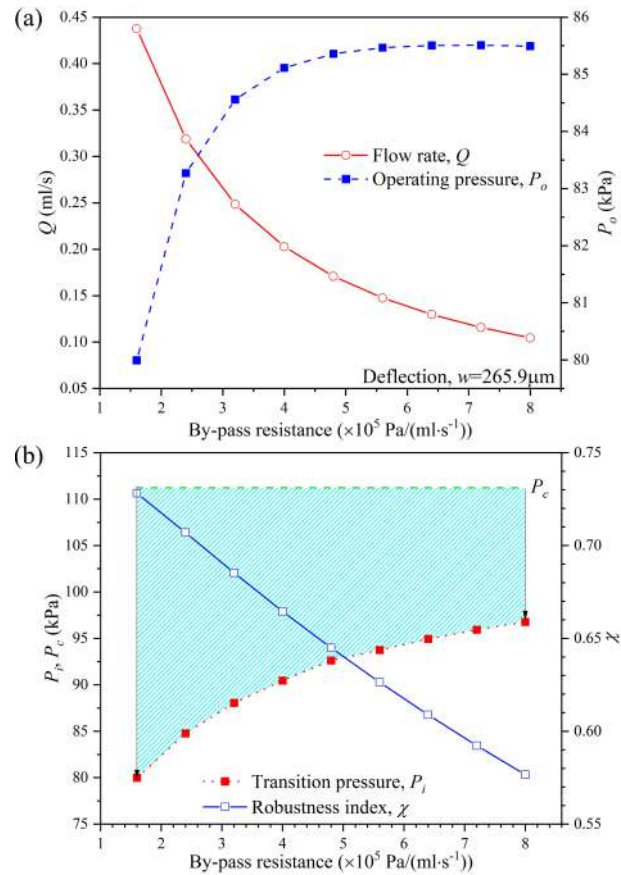


Figure 4: (a) The flow rate  $Q$  and operating pressure  $P_o$  versus  $R_c$  at diaphragm deflection of  $w = 265.9 \mu\text{m}$ . (b) Change of the corresponding transition pressure  $P_t$ , the close pressure  $P_c$  and robustness index  $\chi$  as a function of  $R_c$ . The applied fluid viscosity is 1cP.

necessary for the transition to oscillation. Instead, it will turn directly from a stable flow state into the valving state where the diaphragm goes to the bottom of the oscillation chamber and blocks the outlet. For the by-pass channel of fixed dimensions,  $R_c$  also increases with the viscosity of applied fluid (see Eq. (2.1)), and so reduces the robustness index  $\chi$ . The influence of fluid viscosity will be further discussed in Section 4.3.

#### 4.2 Influence of the pressure-variant resistor ( $\tilde{R}$ )

The characteristics of the pressure-variant resistor  $\tilde{R}$  are determined by several factors, including the material properties, geometries and dimensions of the diaphragm, specifically the radius and thickness of the diaphragm, and the depth of the oscillation chamber. To analyze its influence, the hydraulic diameter of the by-pass channel is fixed at  $D = 200 \mu\text{m}$ , channel length  $l = 8 \text{mm}$ . The other parameters are kept the same as intro-

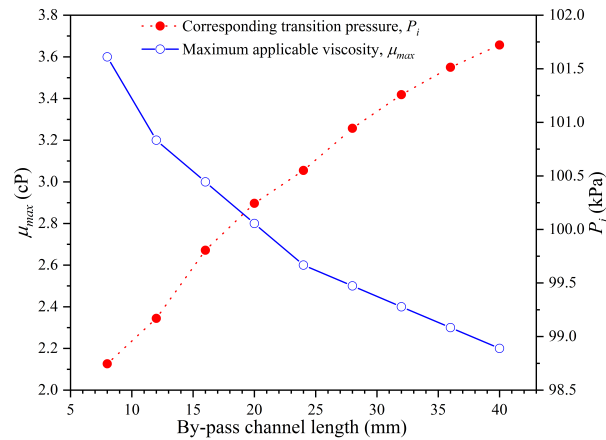


Figure 5: Maximum applicable viscosity  $\mu_{max}$  and the corresponding transition pressure  $P_i$  as a function of the by-pass channel length.

duced in Section 4.1.

#### 4.2.1 Radius $r_0$ and Young's modulus $E$ of the diaphragm

How easily the oscillation diaphragm tends to deflect under a certain load relates to its bending stiffness. It can be adjusted through choosing different materials, or changing the diaphragm's radius  $r_0$  and thickness  $t$ . In current work, the influences of the radius ( $r_0$ ) and the Young's modulus ( $E$ ) of the diaphragm are examined.

Fig. 6(a) plots the results of  $R_{dif}$  versus deflection  $w$  at different  $r_0$ . As  $r_0$  increases, the span of Region III gradually narrows down. At  $r_0 = 0.8mm$ , Region III ranges from  $w = 264.1\mu m$  ( $A_1$ ) to  $w = 321.6\mu m$  ( $A_2$ ),  $\Delta w = 57.5\mu m$ . But at  $r_0 = 1.2mm$ , it decreases to just  $7.3\mu m$  (from point  $B_1$  to  $B_2$ ). When  $r_0$  is further increased to  $1.3mm$ ,  $R_{dif}$  becomes negative over the whole deflection range beyond the transition point ( $w > w_i$ ). The robustness index  $\chi$  becomes zero. Fig. 6(b) shows that the transition pressure  $P_i$ , the close pressure  $P_c$  and  $\chi$  decrease with  $r_0$ .  $P_i$  drops from  $122.3kPa$  to  $27.4kPa$ ,  $P_c$  decreases from  $188.1kPa$  to  $32.3kPa$ . This is because with the increase of  $r_0$ , a smaller load is required to deflect the diaphragm to the transition point. The operating pressure range ( $\Delta P$ ) over the oscillation regime is also reduced. Accordingly, the robustness index  $\chi$  declines from  $0.81$  to  $0.17$ .

Figs. 7(a) and (b) show the influence of Young's modulus ( $E$ ) of the diaphragm. First, the transition pressure  $P_i$  and the close pressure  $P_c$  increase with  $E$ . Over the analyzed range from  $0.76Mpa$  to  $6.08Mpa$ , for fluid of viscosity  $\mu = 2.5cP$ ,  $P_i$  increases from  $49.3kPa$  to  $335.9kPa$  and  $P_c$  goes up from  $55.6kPa$  to  $444.9kPa$ . The operating pressure range  $\Delta P$  expands from  $6.3kPa$  to  $109.0kPa$ . This is consistent with the change of  $\chi$ , which increases from  $0.11$  to  $0.68$ . As the oscillator becomes more robust, the maximum applicable viscosity  $\mu_{max}$  is also increased. It is elevated from  $2.5cP$  to  $7.2cP$ . At the same time, the corresponding transition pressure  $P_i$  increases from  $49.3kPa$  to  $395.0kPa$ . This trend agrees

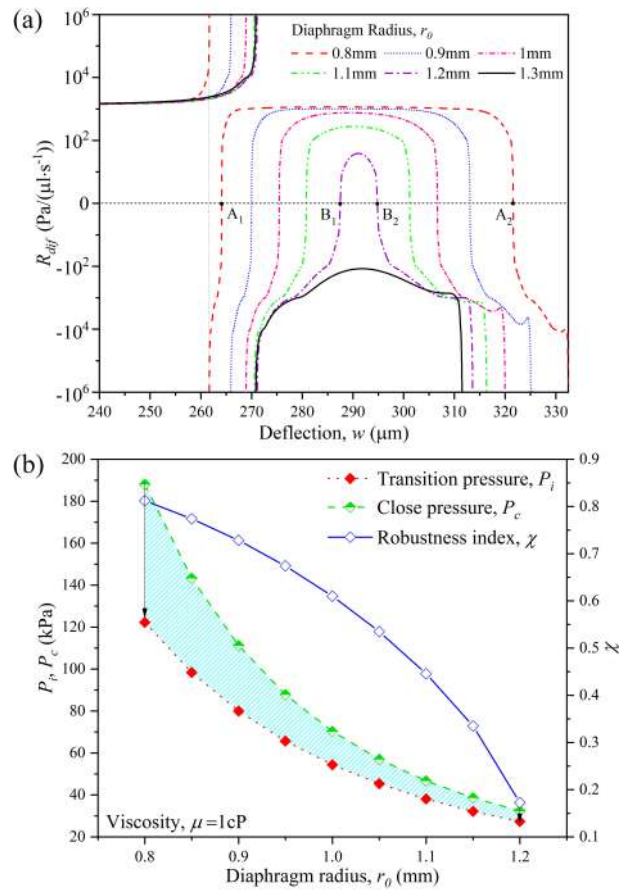


Figure 6: (a) The differential resistance  $R_{dif}$  as a function of the oscillation chamber radius ( $r_0$ ).  $A_1$ ,  $A_2$  and  $B_1$ ,  $B_2$  indicate the span of region III for  $r_0=0.8\text{mm}$  and  $1.2\text{mm}$ . Type II instability is observed at  $r_0=1.3\text{mm}$ . (b) The line chart shows how the transition pressure  $P_i$ , close pressure  $P_c$  and the robustness index  $\chi$  change with  $r_0$ . The applied fluids viscosity is 1cP.

well with previous experimental observation that both  $\mu_{\max}$  and  $P_i$  increase with the diaphragm thickness [15]. Apparently, with the increase of  $E$ , a high pressure is required to deflect the diaphragm, and the flow rate also increases accordingly.

#### 4.2.2 Oscillation chamber depth $H$

The diaphragm deflection  $w$  coupling with the chamber depth  $H$  determines the pressure-variant resistance  $\tilde{R}$ . So the device performance can also be tuned through changing  $H$ . Relevant results are shown in Figs. 8 and 9. With the increases of  $H$ , the diaphragm must deflect further downstream to reach the transition point. At the same time, the span of Region III is increased (refer to Fig. 8(a)). From Fig. 8(b), both  $P_i$  and  $P_c$ , as well as  $\chi$  increase with  $H$ . Over the range of  $H$  from  $200\mu\text{m}$  to  $500\mu\text{m}$ ,  $P_c$  increases from 65.5kPa

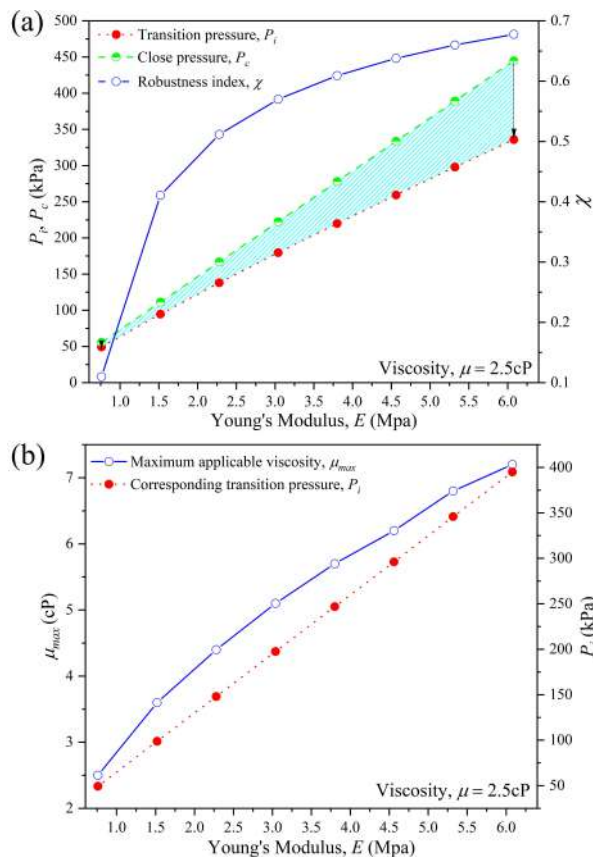


Figure 7: Influences of the diaphragm's Young's modulus on: (a), the transition pressure  $P_i$ , close pressure  $P_c$  and the robustness index  $\chi$ ; (b), the maximum applicable viscosity  $\mu_{\max}$  and the corresponding transition pressure  $P_i$ .

to 254.8kPa and the oscillation pressure range ( $\Delta P$ ) increases from 17.6kPa to 87.8kPa.  $\chi$  increases from 0.48 and 0.87.

It is noted that increasing  $H$  produces similar effects as increasing the Young's modulus of the diaphragm  $E$ . Both the maximum applicable fluid viscosity  $\mu_{\max}$  and the corresponding transition pressure  $P_i$  grow with  $H$ . From Fig. 9(a), for a  $200\mu\text{m}$ -deep chamber,  $\mu_{\max}$  is 1.6cP. For  $500\mu\text{m}$ ,  $\mu_{\max}$  increases to 11.1cP. The corresponding  $P_i$  increases from 52.6kPa to 241.6kPa. At same fluid viscosity, the maximum flow rate  $Q_{\max}$  and  $P_i$  also increase with  $H$ . Refer to Fig. 9(b),  $Q_{\max}$  has increased from 0.26ml/s to 0.89ml/s, and  $P_i$  rises up from 47.9kPa to 167.0kPa.

Though increasing the chamber depth can lift the upper limit of the applicable fluid viscosity and flow rate, attention should be paid that  $H$  must be limited below the yield point of the diaphragm. Otherwise, it will cause permanent deformation of the diaphragm and hence failure of the oscillator.

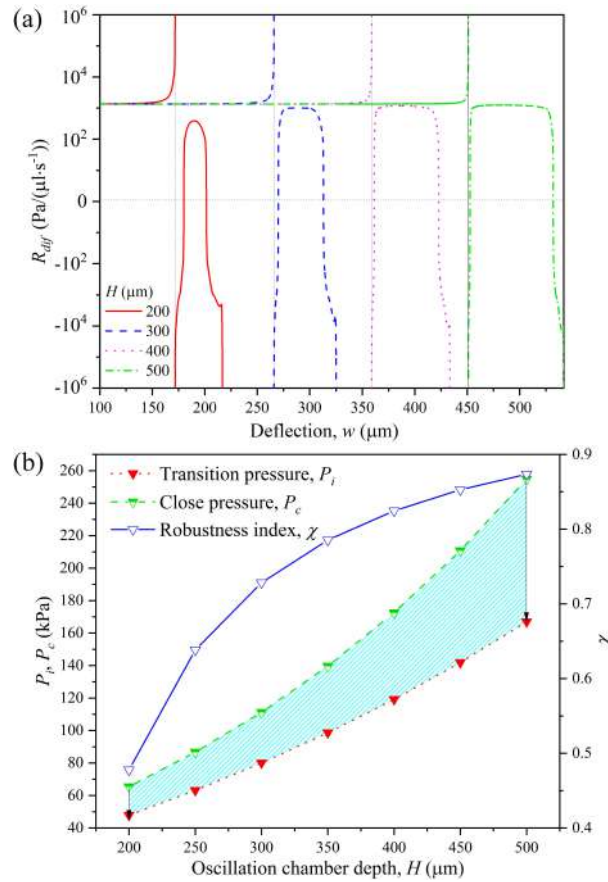


Figure 8: (a) The  $R_{dif}$ - $w$  patterns at different oscillation chamber depths  $H$ . (b) The evolution of transition pressure  $P_i$ , close pressure  $P_c$  and robustness index  $\chi$  with  $H$ .

### 4.3 Influence of the fluid viscosity ( $\mu$ )

Figs. 10 and 11 present the results of two different designs showing the influence of the fluid viscosity. The diaphragm material is the same as that used in Section 4.1. The diaphragm thickness  $t$  is  $500\mu\text{m}$ , radius  $r_0$  is  $1.5\text{mm}$ . The oscillation chamber depth  $H$  is  $900\mu\text{m}$ . The by-pass channel length  $l$  is  $8\text{mm}$  and the hydraulic radius  $D$  is  $200\mu\text{m}$ . For the first design in Fig. 10, the outlet radius ( $r_{out}$ ) is  $250\mu\text{m}$ . Over the fluid viscosity  $\mu$  range from  $1.0\text{cP}$  to  $6.5\text{cP}$ , the maximum flow rate  $Q_{max}$  drops from  $1.70\text{ml/min}$  to  $0.32\text{ml/min}$ , while the transitional operating pressure  $P_i$  increases from  $333.9\text{kPa}$  to  $374.5\text{kPa}$ . For the second design in Fig. 11,  $r_{out}$  is reduced to  $150\mu\text{m}$  while other design parameters remain unchanged.  $Q_{max}$  drops from  $1.53\text{ml/min}$  to  $0.39\text{ml/min}$  as  $\mu$  is increased from  $1.0\text{cP}$  to  $5.0\text{cP}$ . However, for  $P_i$  it exhibits an opposite trend in comparison with the first case. It drops from  $502.9\text{kPa}$  to  $360.6\text{kPa}$  as  $\mu$  rises.

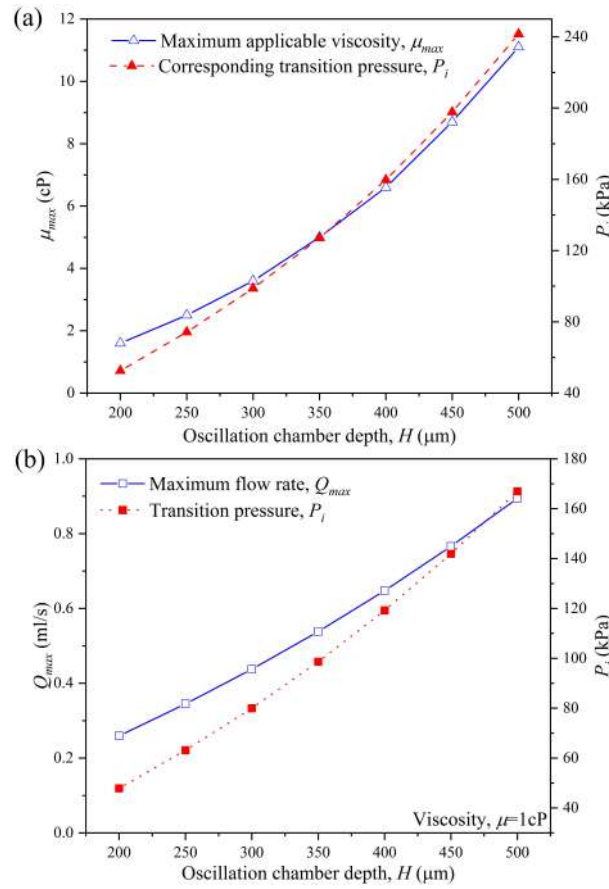


Figure 9: The influence of oscillation chamber depth  $H$  on (a) maximum applicable viscosity  $\mu_{max}$  and corresponding pressure  $P_i$ ; (b) maximum flow rate  $Q_{max}$  and transition pressure  $P_i$  at fluid viscosity of  $1\text{cP}$ .

Interestingly, it is found that for both the cases shown in Figs. 10(b) and 11(b), all the  $P_o-w$  curves at different viscosities cross at a same point  $A$ . Before point  $A$ ,  $P_o$  decreases with  $\mu$ ; afterwards  $P_o$  increases with  $\mu$ . This can be explained as follows. For the operating pressure, Eq. (2.2) can be rewritten as,

$$P_o = Q(R_c + \tilde{R} + R_l) + \frac{\rho U_o^2}{2}. \tag{4.1}$$

Part of the input energy is utilized to overcome the flow resistance, the rest converts to the kinetic energy of the fluid.

For the elastic diaphragm, the total pressure load ( $P_l$ ) attributes to two parts:

$$P_l = P_b + P_{eq}, \tag{4.2}$$

where  $P_b$  is the bias pressure,  $P_{eq}$  is an equivalent pressure load due to Bernoulli effect.

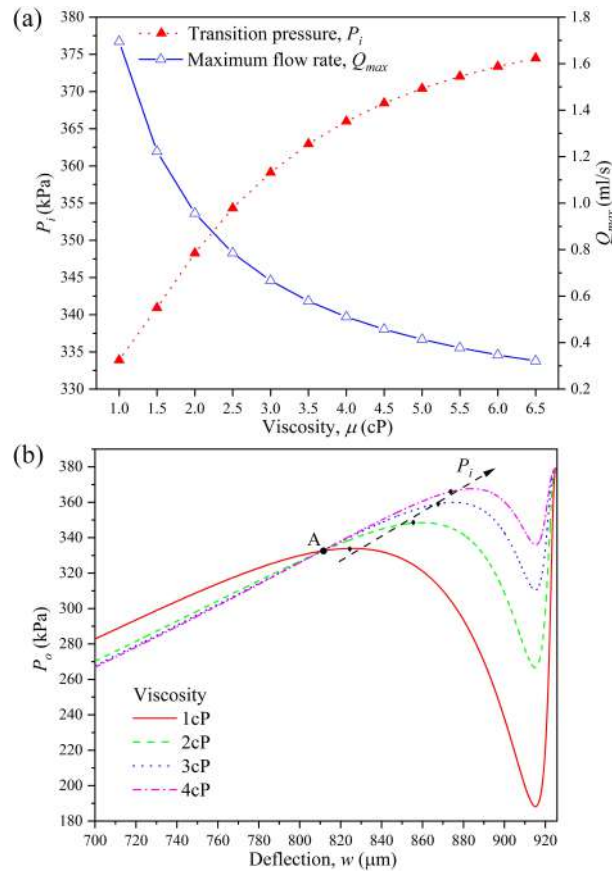


Figure 10: (a) The results of transition pressure  $P_i$  and maximum flow rate  $Q_{max}$  at different fluid viscosities. (b) The plot of operating pressure  $P_o$  as a function of deflection  $w$  at different fluid viscosities. The outlet radius of the oscillator is  $250\mu m$ .

In the low- $w$  range, Bernoulli effect and  $P_{eq}$  can be neglected, the diaphragm deflection is mainly determined by the bias pressure  $P_b = Q(R_c + \tilde{R})$ . For two cases of different viscosities, when the diaphragm deflects to a same position,  $P_{b1} = P_{b2}$ . It can be derived that for both the cases, the item  $Q(R_c + \tilde{R} + R_l)$  also remains the same. Suppose  $\mu_1 < \mu_2$ , then  $Q_1 > Q_2$ . From Eq. (4.1),

$$P_{o,1} - P_{o,2} = \frac{\rho(U_1^2 - U_2^2)}{2} = \frac{\rho(Q_1^2 - Q_2^2)}{2s^2} > 0, \tag{4.3}$$

where  $s$  is the cross sectional area of the outlet. It explains why at low diaphragm deflections before point A, the operating pressure decreases with the fluid viscosity.

In high- $w$  range, Bernoulli effect and  $P_{eq}$  become significant. At the same time, the variant resistance  $\tilde{R}$  increases rapidly,  $R_c + \tilde{R} \gg R_l$ , that is,  $Q(R_c + \tilde{R} + R_l) \approx P_b$ . Then, by

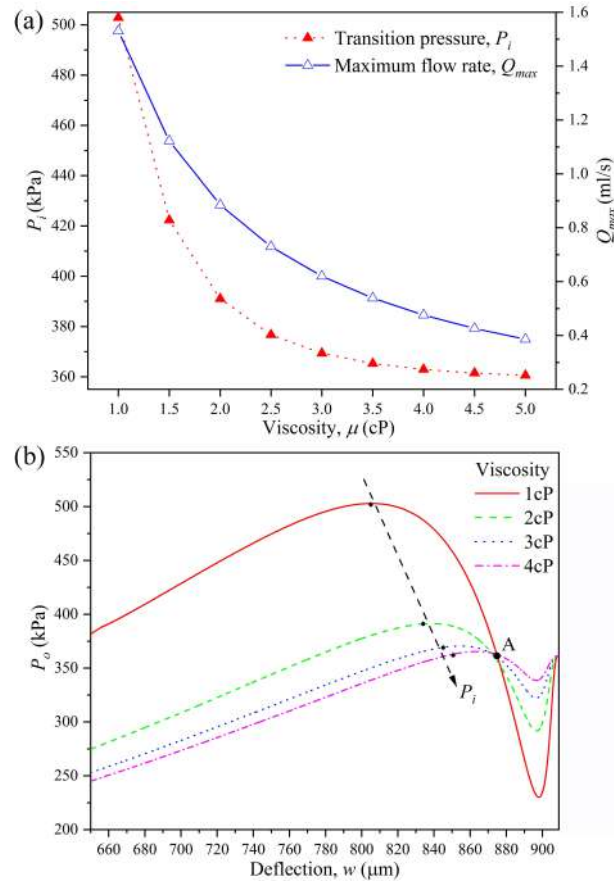


Figure 11: Results of the oscillator with reduced outlet radius,  $r_{out} = 150\mu\text{m}$ . Other design parameters remain the same as that in Fig. 10. (a) Transition pressure  $P_i$  and the maximum flow rate  $Q_{max}$  versus fluid viscosity  $\mu$ . (b) Results of the operating pressure  $P_o$  versus deflection  $w$  at different fluid viscosities.

combining Eqs. (4.1) and (4.2), we obtain

$$P_o \approx P_l - P_{eq} + \frac{\rho U_o^2}{2}. \tag{4.4}$$

Since  $P_{eq}$  is caused by the Bernoulli effect, it relates to the gap between the diaphragm and the chamber bottom. So, it's a function of the diaphragm deflection and can be expressed as  $f(w) \cdot (\frac{\rho Q^2}{2})$  (see Eq. (3.4)). The kinetic pressure term in Eq. (4.4),  $\frac{\rho U_o^2}{2}$  can also be written in the format of  $C_0 \cdot (\frac{\rho Q^2}{2})$ , where  $C_0 = \frac{1}{s^2}$ . With the increase of  $w$  from zero to  $w_m$ , there must exist a point where  $f(w') = C_0$ . At this point,  $P_{eq} = \frac{\rho U_o^2}{2}$ , then  $P_o \approx P_l|_{w=w'}$ . The operating pressure becomes irrelevant with the fluid viscosity. It approximates to the total pressure load required to reach deflection  $w'$ . That is why all the  $P_o$ - $w$  curves at different viscosities cross nearly a same point.

Depending on the design, the intersection point  $A$  may occur either before or after the transition point. As demonstrated here, when the outlet radius  $r_{out}$  is reduced from  $250\mu m$  to  $150\mu m$ , point  $A$  shifts from before to after the transition point. Accordingly, the transition pressure  $P_i$  increases for the former and decreases for the latter with the increase of the fluid viscosity  $\mu$ . This provides an explanation for previous experimental observations. For the oscillator that utilizes silicone rubber for the oscillating diaphragm [14],  $P_i$  increases with  $\mu$ ; while for another design using elastic metal [15], the trend becomes opposite. It is believed that for the latter, the increase in fluid viscosity have caused a more significant reduction in the flow rate and the kinetic pressure. As a result, the required operating pressure is reduced.

## 5 Conclusions and discussions

In this work, the underlying physics and parameter influences of a NDR fluidic oscillator are systematically studied through quasi-static analysis using an equivalent-circuit-model. First, the Bernoulli effect is identified to play an important role. It is the key reason leading to the  $N$ -shaped  $P_b$ - $w$  curve, which is essential to trigger the oscillation. For the cases where the Bernoulli effect becomes very weak, e.g., when a highly viscous fluid is applied, the bias pressure  $P_b$  will monotonically increases with the diaphragm deflection  $w$ . The device exhibits a second type of instability. The oscillation can hardly occur. Instead, it will directly transit from the laminar-flow state to the valving state. Based on the evolution of the differential resistance with the diaphragm deflection (the  $R_{dif}$ - $w$  curve), an empirical robustness index  $\chi$  is defined, and the design space of the NDR oscillator is explored.

Parameter studies show that the robustness of the NDR oscillator can be improved through reducing the by-pass resistance  $R_c$ , increasing the depth of the oscillation chamber  $H$ , or increasing the bending stiffness of the diaphragm. On the contrary, the robustness will deteriorate. With the increase of  $\chi$ , the operating pressure range is expanded, the upper limit of the applicable fluid viscosity is improved, and the maximum flow rate is increased. For the transition pressure  $P_i$ , it increases with  $R_c$ ,  $H$ , Young's modules of the diaphragm  $E$ , but decreases with diaphragm radius  $r_0$ . The outlet radius  $r_{out}$  influences how much of the operating pressure will be converted to the kinetic pressure, depending on which the transition pressure may either increases or decrease with the fluid viscosity. All these findings will help to advance the understanding of the NDR oscillation in microfluidic networks, and provide useful design guidelines of the NDR oscillator to meet various application requirements.

Lastly, it should be noted that in the current static analysis the influences of the fluidic inductor and capacitor are neglected. They are key parameters that determine the oscillation frequency. In the dynamic state, the inductance and capacitance load will also influence the working pressure range and fluid viscosity range. In its practical operation, the oscillator can still work within a certain pressure range above  $P_c$ . This is because in

the dynamic state, collision occurs when the elastic diaphragm hits the chamber bottom. The elastic force can overcome the upstream pressure and push the diaphragm back. For a more detailed analysis of the NDR oscillator, all above issues should be taken into consideration, which require further exploration.

## Acknowledgements

This work was supported in part by the National Natural Science Foundation of China (No. 51575282), the Fundamental Research Funds for the Central Universities (Nos. 30915118803 and 30916012101), Postgraduate Research & Practice Innovation Program of Jiangsu Province (No. KYCX20\_0266), Nanyang Technological University and Singapore Institute of Manufacturing Technology, under the Agency for Science, Technology and Research (A\*STAR, Singapore).

## References

- [1] P. A. AUROUX, D. IOSSIFIDIS, D. R. REYES AND A. MANZ, *Micro total analysis systems. 2. analytical standard operations and applications*, *Anal. Chem.*, 74 (2002), pp. 2637–2652.
- [2] K. S. ELVIRA, X. C. I. SOLVAS, R. C. R. WOOTTON AND A. J. DEMELLO, *The past, present and potential for microfluidic reactor technology in chemical synthesis*, *Nat. Chem.*, 5 (2013), pp. 905–915.
- [3] T. M. SQUIRES AND S. R. QUAKE, *Microfluidics: Fluid physics at the nanoliter scale*, *Rev. Mod. Phys.*, 77 (2005), pp. 977–1026.
- [4] P. LI, Z. MAO AND Z. PENG, ET AL., *Acoustic separation of circulating tumor cells*, *Proc. Natl. Acad. Sci. USA*, 112 (2015), pp. 4970–4975.
- [5] T. YANG, Y. CHEN AND P. MINZIONI, *A review on optical actuators for microfluidic systems*, *J. Micromech. Microeng.*, 27 (2017), pp. 123001–123019.
- [6] H. LIU, Z. WEN, Y. XU, Z. SHANG, J. LAN AND P. TIAN, *An integrated microfluidic analysis microsystems with bacterial capture enrichment and in-situ impedance detection*, *Mod. Phys. Lett. B*, 31 (2017), 1750233.
- [7] S. L. STOTT, C. HSU, D. I. TSUKROV, ET AL., *Isolation of circulating tumor cells using a microvortex-generating herringbone-chip*, *Proc. Natl. Acad. Sci. USA*, 107 (2010), pp. 18392–18397.
- [8] J. ZHANG, S. YAN, D. YUAN, G. ALICI, N. T. NGUYEN, M. E. WARKIANI AND W. LI, *Fundamentals and applications of inertial microfluidics: A review*, *Lab Chip*, 16 (2016), pp. 10–34.
- [9] F. C. PANWALA, R. KUMAR AND P. M. SHAKEEL, *An analysis of bacteria separation and filtration from blood sample using passive methods*, *Measurement*, 140 (2019), pp. 29–46.
- [10] D. C. LESLIE, C. J. EASLEY, E. SEKER, J. M. KARLINSEY, M. UTZ, M. R. BEGLEY AND J. P. LANDERS, *Frequency-specific flow control in microfluidic circuits with passive elastomeric features*, *Nat. Phys.*, 5 (2009), pp. 231–235.
- [11] B. MOSADEGH, C. H. KUO, Y. C. TUNG, Y. S. TORISAWA, T. BERSANO-BEGEY, H. TAVANA AND S. TAKAYAMA, *Integrated elastomeric components for autonomous regulation of sequentia and oscillatory flow switching in microfluidic devices*, *Nat. phys.*, 6 (2010), pp. 433–437.

- [12] Y. J. KANG AND S. YANG, *Fluidic low pass filter for hydrodynamic flow stabilization in microfluidic environments*, *Lab Chip*, 12 (2012), pp. 1881–1889.
- [13] S. J. KIM, R. YOKOKAWA AND S. TAKAYAMA, *Analyzing threshold pressure limitations in microfluidic transistors for self-regulated microfluidic circuits*, *Appl. Phys. Lett.*, 101 (2012), 234107.
- [14] H. M. XIA, Z. P. WANG, W. FAN, A. WIJAYA, W. WANG AND Z. F. WANG, *Converting steady laminar flow to oscillatory flow through a hydroelasticity approach at microscales*, *Lab Chip*, 12 (2012), pp. 60–64.
- [15] H. M. XIA, Z. P. WANG, V. B. NGUYEN, S. H. NG, W. WANG, F. Y. LEONG AND D. V. LE, *Analyzing the transition pressure and viscosity limit of a hydroelastic microfluidic oscillator*, *Appl. Phys. Lett.*, 104 (2014), 024101.
- [16] Y. Y. ZHANG, H. M. XIA, J. W. WU, J. ZHANG AND Z. P. WANG, *Synchronized generation and coalescence of largely dissimilar microdroplets governed by pulsating continuous-phase flow*, *Appl. Phys. Lett.*, 114 (2019), 073701.
- [17] J. M. WANG, Q. Q. JIN, Y. Y. ZHANG, H. C. FAN AND H. M. XIA, *Reducing the membrane fouling in cross-flow filtration using a facile fluidic oscillator*, *Sep. Purif. Technol.*, 272 (2021), 118854.
- [18] J. W. WU, H. M. XIA, Y. Y. ZHANG, S. F. ZHAO, P. ZHU AND Z. P. WANG, *An efficient micromixer combining oscillatory flow and divergent circular chamber*, *Microsyst. Technol.*, 25 (2019), pp. 2741–2750.
- [19] J. W. WU, H. M. XIA AND Y. Y. ZHANG, *Microfluidic mixing through oscillatory transverse perturbations*, *Mod. Phys. Lett. B*, 32 (2018), 1840030.
- [20] H. M. XIA, Y. P. SEAH, Y. C. LIU, W. WANG, A. G. G. TOH AND Z. P. WANG, *Anti-solvent precipitation of solid lipid nanoparticles using a microfluidic oscillator mixer*, *Microfluid. Nanofluid.*, 19 (2015), pp. 283–290.
- [21] S. F. ZHAO, J. W. WU, P. ZHU, H. M. XIA, C. CHEN AND R. Q. SHEN, *Microfluidic Platform for Preparation and Screening of Narrow Size-Distributed Nanoscale Explosives and Supermixed Composite Explosives*, *Ind. Eng. Chem. Res.*, 57 (2018), pp. 13191–13204.
- [22] M. J. SHELLEY AND J. ZHANG, *Flapping and bending bodies interacting with fluid flows*, *Annu. Rev. Fluid Mech.*, 43 (2011), pp. 449–465.
- [23] V. ESFAHANIAN, E. DEHDASHTI AND A. M. DEHROUYEH-SEMNANI, *Fluid-Structure Interaction in microchannel using Lattice Boltzmann method and size-dependent beam element*, *Adv. Appl. Math. Mech.*, 6 (2014), pp. 345–358.
- [24] P. WANG AND D. LU, *Nonlinear hydroelastic waves traveling in a plate in terms of Plotnikov-Toland's model*, *Adv. Appl. Math. Mech.*, 13 (2021), pp. 724–734.
- [25] H. M. XIA, J. W. WU AND Z. P. WANG, *The negative-differential-resistance (NDR) mechanism of a hydroelastic microfluidic oscillator*, *J. Micromech. Microeng.*, 27 (2017), 075001.
- [26] G. O. BROWN, *The history of the Darcy-Weisbach equation for pipe flow resistance*, *Environ. Water. Resour. Hist.*, (2003), pp 34–43.